Comprehensive mean-field analysis of magnetic and charge orders in the two-dimensional Hubbard model

Robin Scholle ⬤, Pietro M. Bonetti ⬤, Demetrio Vilardi, and Walter Metzner ⬤

Max Planck Institute for Solid State Research, D-70569 Stuttgart, Germany

We present an unbiased mean-field analysis of magnetic and charge orders in the two-dimensional Hubbard model on a square lattice, at both zero and finite temperatures. Unrestricted Hartree-Fock calculations on large finite lattices are complemented by solutions restricted to Néel and circular spiral order in the thermodynamic limit. The magnetic states are classified by a systematic scheme based on the dominant Fourier components of the spin texture. On finite lattices a whole zoo of ordering patterns appears. We show that many of these states are finite-size artifacts related to the limited choice of ordering wave vectors on a finite lattice. In the thermodynamic limit only three classes of states with a relatively simple structure survive: Néel, circular spiral, and stripe states. Stripes involve also charge order and can be unidirectional or bidirectional, with horizontal and/or vertical orientation. We present complete phase diagrams in the plane spanned by electron density and temperature, for a moderate Hubbard interaction and various choices of the next-nearest-neighbor hopping amplitude.

I. INTRODUCTION

The two-dimensional Hubbard model is a prototype for competing ordering tendencies in interacting electron systems. It captures key features of the valence electrons in high-T_c cuprates such as antiferromagnetism and d-wave superconductivity [1]. In spite of substantial progress in the development of quantum many-body methods, only fragments of the phase diagram of this important model have been established [2,3].

There is no doubt that at half filling the ground state of the two-dimensional Hubbard model with pure nearest-neighbor hopping is a Néel-ordered antiferromagnet for any repulsive Hubbard interaction $U > 0$, and beyond a certain critical repulsion if hopping amplitudes beyond nearest neighbors are present. However, for electron densities below half filling the Néel state quickly becomes unstable [4–7], leading to other magnetic states or possibly phase separation. These states are usually metallic and thus prone to pairing instabilities.

There is a whole zoo of possible magnetic states. Except for the Néel state, most of them are characterized by one or several ordering wave vectors which are generically incommensurate with the lattice periodicity. Many approximate calculations point toward planar circular spirals [4–16] and collinear spin density waves [17–29] as the most important candidates. The latter entail charge order with regions of reduced charge density arranged along one-dimensional lines, and are therefore also known as "spin-charge stripes" [30].

By contrast, the charge distribution of (circular) spiral states remains uniform.

Recently, exact numerical calculations on finite lattices have provided strong evidence for stripe order in the ground state of the Hubbard model with pure nearest-neighbor hopping and large U for special hole-doping fractions: 1/10 and 1/8, corresponding to electron densities 0.9 and 0.875, respectively [31,32]. No superconductivity was found in these cases. However, allowing for next-nearest-neighbor hopping, superconductivity reemerges for a range of densities away from half filling [33]. Exact numerical evaluations at finite temperatures yield peaks in the spin susceptibility at the Néel wave vector (π, π) near half filling, and peaks at incommensurate wave vectors in the spin and charge susceptibility for sufficiently large hole doping [34,35].

Unlike superconductivity, magnetic order in the (repulsive) Hubbard model can be captured already within a static mean-field approximation, also known as Hartree-Fock theory. While the size of the order parameter and the regime of ordered states in the phase diagram are grossly overestimated by mean-field theory, finite-size effects can be studied in more detail because much larger lattices can be dealt with. For Néel, circular spiral, and stripe states, mean-field calculations can be performed directly in the thermodynamic limit, albeit only for wave vectors commensurate with the lattice in the case of stripes. Indeed, numerous Hartree-Fock studies of the two-dimensional Hubbard model have already appeared. However, in many of them the magnetic states were restricted to ferromagnetic and Néel [36–38], or spiral order [11,12]. The latter includes ferromagnetic and Néel states as the special cases with wave vectors $(0,0)$ and (π, π), respectively. For small hole doping, this restriction often leads to phase separation in paramagnetic, ferromagnetic, and antiferromagnetic regions [11,12,38]. Allowing for arbitrary collinear spin order or even for completely arbitrary spin

configurations—combined with charge order—spin-charge stripes have been found [17–22,27,29].

With very few exceptions, Hartree-Fock studies of the two-dimensional Hubbard model have been limited to the ground state. At finite temperatures, any magnetic order is prohibited by thermal fluctuations, as is rigorously established by the Mermin-Wagner theorem [39]. Magnetic states obtained in the Hartree-Fock approximation at finite temperatures obviously violate this theorem. However, such states become meaningful as an ingredient for theories of fluctuating magnetic order, where the electron is fractionalized into a "chargon" with a magnetically ordered pseudospin, and a fluctuating spin rotation matrix, which restores the SU(2) spin symmetry of the electronic state [40–42]. The "handshake" between magnetic order found in the ground state and magnetic correlations at finite temperatures has attracted much interest recently, and there has been some progress in attempts to close the gap between exact numerical solutions obtained from zero- and finite-temperature algorithms [35,43–45].

In this paper we perform a comprehensive and completely unrestricted Hartree-Fock study of the two-dimensional Hubbard model at zero and finite temperatures. We choose a moderate interaction strength and analyze a broad range of electron densities below, at, and above half filling. We consider both the "pure" Hubbard model, with pure nearest-neighbor hopping t, as well as its physically more relevant extension with next-nearest-neighbor hopping t'. Unrestricted real-space calculations on large lattices (from 20×20 to 48×48) are complemented by momentum-space calculations for Néel and spiral states in the thermodynamic limit.

As our main result we present three complete mean-field phase diagrams spanned by density and temperature, for three choices of t'/t. All of them contain Néel, spiral, and stripe states, where, for $t' \leqslant -0.15$, the latter two are confined to the hole-doped region (below half filling). Other, more complex magnetic states appearing in the real-space calculations could be identified as finite-size artifacts, which are related to the restricted discrete choice of ordering wave vectors on the finite lattice. The momentum-space calculations for Néel and spiral states are consistent with the real-space calculations, and instabilities toward stripe states are signaled by a divergence of the spin-charge susceptibility in the spiral state.

The remainder of the paper is structured as follows. In Sec. II we describe the real-space mean-field theory, and in Sec. III we present our results. In the Conclusion, in Sec. IV, we provide a summary and outlook. Some details regarding the calculations and classification of states are described in two Appendixes.

II. MODEL AND METHOD

The Hubbard Hamiltonian for spin-$\frac{1}{2}$ fermions with intersite hopping amplitudes $t_{jj'}$ and a local interaction U reads

$$H = H_0 + H_{\text{int}} = \sum_{j,j',\sigma} t_{jj'} c_{j\sigma}^\dagger c_{j'\sigma} + U \sum_j n_{j\uparrow} n_{j\downarrow}, \quad (1)$$

where $c_{j\sigma}$ ($c_{j\sigma}^\dagger$) annihilates (creates) an electron on lattice site j with spin orientation $\sigma \in \{\uparrow, \downarrow\}$, and $n_{j\sigma} = c_{j\sigma}^\dagger c_{j\sigma}$. The

hopping matrix $t_{jj'}$ depends only on the distance between the sites j and j', and it is parametrized by $-t$ if j and j' are nearest-neighbor sites, and by $-t'$ if j and j' are next-to-nearest neighbors. We consider only the repulsive Hubbard model where U is positive. In the following, we use the nearest-neighbor hopping amplitude t as our energy unit; that is, we set $t = 1$.

A. Real-space mean-field theory

In the mean-field (or Hartree-Fock) approximation, the interaction part of the Hamiltonian H_{int} is replaced by an effective quadratic (in c, $c^\dagger$) operator. Following Zaanen and Gunnarsson [18], we decouple H_{int} as

$$H_{\text{int}}^{\text{MF}} = \sum_{j\sigma} \Delta_{j\bar{\sigma}} n_{j\sigma} + \sum_j (\Delta_{j-} c_{j\uparrow}^\dagger c_{j\downarrow} + \Delta_{j+} c_{j\downarrow}^\dagger c_{j\uparrow})$$
$$- \frac{1}{U} \sum_j (\Delta_{j\uparrow} \Delta_{j\downarrow} - \Delta_{j-} \Delta_{j+}), \quad (2)$$

with the convention $\bar{\uparrow} = \downarrow$ and $\bar{\downarrow} = \uparrow$. The parameters $\Delta_{j\alpha}$ are self-consistently determined by the "gap equations"

$$\Delta_{j\sigma} = U \langle n_{j\sigma} \rangle, \quad (3a)$$

$$\Delta_{j+} = \Delta_{j-}^* = -U \langle c_{j\uparrow}^\dagger c_{j\downarrow} \rangle. \quad (3b)$$

The decoupling in Eq. (2) allows for arbitrary spin and charge patterns. In most of the previous mean-field studies of the Hubbard model, only the first (Hartree) or the second (Fock) term on the right-hand side of Eq. (2) has been considered, restricting the spin order to collinear or spiral order, respectively.

We iteratively solve the mean-field equations on a finite square lattice with $\mathcal{N}_x$ ($\mathcal{N}_y$) sites in the x (y) direction and periodic boundary conditions. We denote the total number of lattice sites by $\mathcal{N} = \mathcal{N}_x \mathcal{N}_y$.

The mean-field Hamiltonian can be written as

$$H^{\text{MF}} = H_0 + H_{\text{int}}^{\text{MF}} = \sum_{j,j'} \sum_{\sigma,\sigma'} c_{j\sigma}^\dagger \mathcal{H}_{jj'}^{\sigma\sigma'} c_{j'\sigma'} + \text{const}, \quad (4)$$

where $\mathcal{H}_{jj'}^{\sigma\sigma'} \in \mathbb{C}^{2\mathcal{N} \times 2\mathcal{N}}$ is a square matrix with $4\mathcal{N}$ real parameters to be determined self-consistently ($\Delta_{j\uparrow}$, $\Delta_{j\downarrow}$, $\text{Re}\Delta_{j+}$, and $\text{Im}\Delta_{j+}$ for each lattice site). These parameters are related to the expectation values of the charge and spin order parameters by

$$\langle n_j \rangle = \frac{\Delta_{j\uparrow} + \Delta_{j\downarrow}}{U}, \quad (5a)$$

$$\langle S_j^z \rangle = \frac{\Delta_{j\uparrow} - \Delta_{j\downarrow}}{2U}, \quad (5b)$$

$$\langle S_j^x \rangle = -\frac{\Delta_{j+} + \Delta_{j-}}{2U}, \quad (5c)$$

$$\langle S_j^y \rangle = -\frac{\Delta_{j+} - \Delta_{j-}}{2iU}, \quad (5d)$$

where $n_j = n_{j\uparrow} + n_{j\downarrow}$ and $\vec{S}_j = \frac{1}{2} c_j^\dagger \vec{\sigma} c_j$, with $\vec{\sigma}$ being the Pauli matrices.

We run calculations at fixed density n; that is, we enforce the constraint $\frac{1}{\mathcal{N}} \sum_{j\sigma} \langle n_{j\sigma} \rangle = n$. In the ground state this is

achieved by calculating the expectation values on the right-hand sides of Eqs. (3)

$$\langle c_{j\sigma}^{\dagger} c_{j\sigma'} \rangle = \sum_{\ell=1}^{N} \left(v_{j\sigma}^{\ell} \right)^{*} v_{j\sigma'}^{\ell}, \tag{6}$$

where N is the total particle number, ℓ labels the $2\mathcal{N}$ eigenvalues ϵ_{ℓ} of $\mathcal{H}_{jj'}^{\sigma\sigma'}$ in ascending order, and $v_{j\sigma}^{\ell}$ is the normalized eigenvector corresponding to the ℓth eigenvalue. In this way, only rational densities of the form $n = N/\mathcal{N}$ are obtained. At finite temperatures $T > 0$, one needs to introduce a chemical potential μ, and Eq. (6) is replaced by

$$\langle c_{j\sigma}^{\dagger} c_{j\sigma'} \rangle = \sum_{\ell=1}^{2\mathcal{N}} \left(v_{j\sigma}^{\ell} \right)^{*} v_{j\sigma'}^{\ell} f(\epsilon_{\ell} - \mu), \tag{7}$$

with $f(x) = 1/(1 + e^{x/T})$ being the Fermi function. The chemical potential is adjusted to enforce the chosen value for the average density

$$\frac{1}{\mathcal{N}} \sum_{j} \langle n_j \rangle = \frac{1}{\mathcal{N}} \sum_{\ell=1}^{2\mathcal{N}} f(\epsilon_{\ell} - \mu) = n, \tag{8}$$

where we have made use of the property $\sum_{j,\sigma} (v_{j\sigma}^{\ell})^{*} v_{j\sigma}^{\ell} = 1$, deriving from the orthonormality condition of the eigenvectors.

We solve our system of equations in the following iterative manner: Starting from a random initial set of parameters $\Delta_{j\alpha}$ with $\alpha \in \{\uparrow, \downarrow, +, -\}$ and $\Delta_{j-} = \Delta_{j+}^{*}$, we plug them into $\mathcal{H}_{jj'}^{\sigma\sigma'}$, from which we compute the eigenvectors and the expectation values in Eq. (3) to update the values of $\Delta_{j\alpha}$. We repeat this procedure until convergence is reached. At finite temperatures, we compute the chemical potential at every iteration from Eq. (8). More details on the numerical implementation can be found in Appendix A.

Within the mean-field approximation, the free energy per lattice site is given by

$$F/\mathcal{N} = -\frac{T}{\mathcal{N}} \sum_{\ell} \ln\left(1 + e^{-\beta(\epsilon_{\ell} - \mu)}\right)$$
$$- \frac{1}{\mathcal{N}U} \sum_{j} (\Delta_{j\uparrow}\Delta_{j\downarrow} - \Delta_{j-}\Delta_{j+}) + \mu n. \tag{9}$$

B. Classification of magnetic orders

In this section we introduce a classification of the distinct magnetic states we find. We classify the different states solely based on their spin pattern, similarly to the classification of Sachdev *et al.* [46]. In agreement with Ref. [46], we generally find that the modulation of the charge density is roughly proportional to the square of the spin amplitudes, that is,

$$\langle n_j \rangle \approx \text{const} \langle \vec{S}_j^2 \rangle + \text{const}, \tag{10}$$

as could be deduced from the lowest-order coupling between the charge and spin density wave order parameters in Landau theory [47].

To identify a state from a (converged) real-space spin pattern defined by the spin expectation values $\langle \vec{S}_j \rangle$, we perform a Fourier transform,

$$\langle \vec{S}_j \rangle = \sum_{\mathbf{q}} \vec{\mathcal{S}}_{\mathbf{q}} \, e^{i\mathbf{q}\cdot\mathbf{r}_j}, \tag{11}$$

where $\vec{\mathcal{S}}_{\mathbf{q}}$ with $\vec{\mathcal{S}}_{\mathbf{q}} = \vec{\mathcal{S}}_{-\mathbf{q}}^{*}$ is the Fourier component of the spins corresponding to the wave vector $\mathbf{q}$, and $\mathbf{r}_j$ represents the real-space coordinate of lattice site j. The sum runs only over the $\mathcal{N} = \mathcal{N}_x \mathcal{N}_y$ momenta allowed by the periodic boundary conditions on the finite-size lattice. Since we are exclusively dealing with even numbers $\mathcal{N}_x$ and $\mathcal{N}_y$, the allowed momenta can be written as

$$\mathbf{q} \in \left\{ \left(\pi - \pi \frac{2v_x}{\mathcal{N}_x}, \pi - \pi \frac{2v_y}{\mathcal{N}_y} \right) \middle| v_\alpha \in \{0, 1, \ldots, \mathcal{N}_\alpha - 1\} \right\}. \tag{12}$$

In the majority of cases only one or two modes with fixed wave vectors $\mathbf{q}$ (together with their partner $-\mathbf{q}$) contribute significantly to $\langle \vec{S}_j \rangle$. Usually, these wave vectors have the form $\mathbf{Q}_x \equiv (\pi - 2\pi\eta_x, \pi)$ and/or $\mathbf{Q}_y \equiv (\pi, \pi - 2\pi\eta_y)$. The parameters η_α are frequently referred to as "incommensurabilities" in the literature. Note that, in a finite system, η_α is restricted to integer multiples of $1/\mathcal{N}_\alpha$ [see Eq. (12)]. For lattices with $\mathcal{N}_x = \mathcal{N}_y$, we always find $\eta_x = \eta_y \equiv \eta$. We also checked for magnetic order with diagonal wave vectors of the form $\mathbf{Q}_{xy} \equiv (\pi - 2\pi\eta, \pi - 2\pi\eta)$, but we rarely found states with these modes as dominant contributions, and these rare instances did not survive when repeating the calculation on a larger lattice.

In cases with only one mode, we can express $\vec{\mathcal{S}}_{\mathbf{q}}$ as

$$\vec{\mathcal{S}}_{\mathbf{q}} = \tfrac{1}{2}(\vec{\mathcal{S}} \, \delta_{\mathbf{q},\mathbf{Q}} + \vec{\mathcal{S}}^{*} \delta_{\mathbf{q},-\mathbf{Q}}), \tag{13}$$

where $\mathbf{Q}$ has the form $\mathbf{Q}_x$ or $\mathbf{Q}_y$. In states with two modes, we have

$$\vec{\mathcal{S}}_{\mathbf{q}} = \tfrac{1}{2}\big(\vec{\mathcal{S}}_x \, \delta_{\mathbf{q},\mathbf{Q}_x} + \vec{\mathcal{S}}_x^{*} \delta_{\mathbf{q},-\mathbf{Q}_x}\big)$$
$$+ \tfrac{1}{2}\big(\vec{\mathcal{S}}_y \, \delta_{\mathbf{q},\mathbf{Q}_y} + \vec{\mathcal{S}}_y^{*} \delta_{\mathbf{q},-\mathbf{Q}_y}\big). \tag{14}$$

In our mean-field calculations we find nine distinct phases. We sketch the spin and charge order pattern for a representative of each phase in Fig. 1. Phases that can be transformed into each other, by a point group symmetry operation of the lattice (rotations and reflections), by a spatial translation (changing the phases of $\vec{\mathcal{S}}_x$ and $\vec{\mathcal{S}}_y$), or by a global SU(2) rotation of the spin frame, belong to the same class. In the following, we describe each class by one of its representatives.

In principle, there might be other possible spin configurations, for example, the phases F and G in the classification of Ref. [46], but we do not find them in the parameter regime chosen in our calculations.

1. Paramagnetism

In the paramagnetic phase the expectation value of the spin on each site vanishes (that is, $\langle \vec{S}_j \rangle = 0$), and the charge distribution is uniform, $\langle n_j \rangle = n$ [see Fig. 1(a)].

2. Néel antiferromagnetism

In a Néel antiferromagnet only $\vec{\mathcal{S}}_{(\pi,\pi)}$ is nonzero. In real space, adjacent spins point in opposite directions, all spins
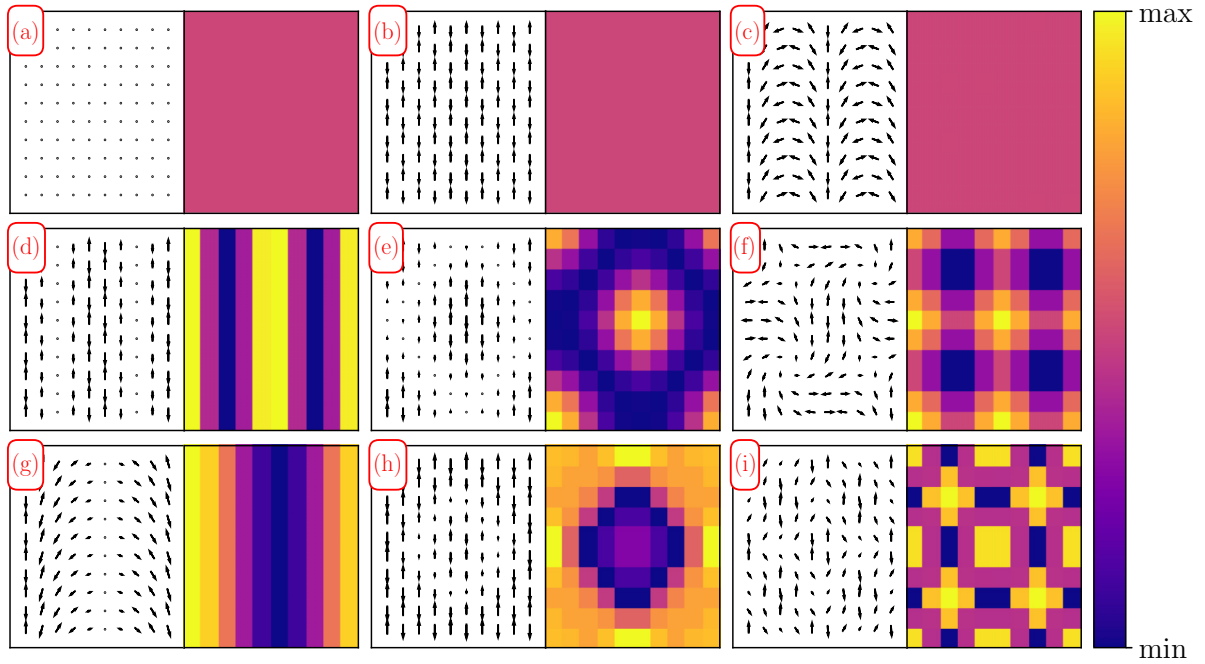
FIG. 1. Overview of the different orders found in our calculations, schematically shown on a 10×10 lattice. In each panel, the square on the left shows the relative spin orientations and amplitudes (length of the arrows) of each phase, where we chose a frame such that the spins lie in the x-y plane and the bottom left spin points along the y direction. The right plot in each panel shows the corresponding charge modulation, using a color code defined on the right edge of the figure. The various panels exemplify the following magnetic orders: (a) paramagnetism, (b) Néel antiferromagnetism, (c) spiral order, (d) stripe order, (e) collinear bidirectional stripe order, (f) coplanar bidirectional stripe order, (g) beat order, (h) other collinear orders, and (i) "strange" order. Only one example of strange order has been shown, while we also find different ones, often with less regular patterns.

have the same amplitude, and the charge is homogeneously distributed, as shown in Fig. 1(b).

3. Spiral

We refer to planar circular spiral states briefly as "spiral" states. Such a state is characterized by a single mode with a wave vector $\mathbf{Q}$, and (as a representative)

$$\vec{\mathcal{S}} = S_0 \begin{pmatrix} 1 \\ i \\ 0 \end{pmatrix}, \tag{15}$$

where S_0 is a real number. In real space, the corresponding spin pattern has the form

$$\langle \vec{S}_j \rangle = S_0 \begin{pmatrix} \cos(\mathbf{Q} \cdot \mathbf{r}_j) \\ \sin(\mathbf{Q} \cdot \mathbf{r}_j) \\ 0 \end{pmatrix}. \tag{16}$$

The spin magnitude $|\langle \vec{S}_j \rangle|$ is constant (independent of j), and the charge distribution is therefore homogeneous, as shown in Fig. 1(c). The wave vector $\mathbf{Q}$ has the form $\mathbf{Q}_x = (\pi - 2\pi\eta, \pi)$ or $\mathbf{Q}_y = (\pi, \pi - 2\pi\eta)$; that is, only one component deviates from π. The Néel state can be viewed as the special case of a spiral with $\mathbf{Q} = (\pi, \pi)$.

4. Unidirectional stripes

A (unidirectional) stripe state is described by a single $\mathbf{q}$ mode such that

$$\vec{\mathcal{S}} = S_0 \begin{pmatrix} 1 \\ 0 \\ 0 \end{pmatrix}. \tag{17}$$

In this state, the spins are ordered collinearly with a modulation along the x (or y) axis. In real space, the spin modulation is given by

$$\langle \vec{S}_j \rangle = S_0 \begin{pmatrix} \cos(\mathbf{Q} \cdot \mathbf{r}_j) \\ 0 \\ 0 \end{pmatrix}. \tag{18}$$

Once again, the wave vector $\mathbf{Q}$ has either the form $\mathbf{Q}_x$ or the form $\mathbf{Q}_y$. The charge order of this state is a unidirectional charge density wave with a wave vector $2\mathbf{Q}$; that is, $\langle n_j \rangle - n \propto \cos(2\mathbf{Q} \cdot \mathbf{r}_j)$. The minima in the amplitude of the spin coincide with the minima of the charge modulation, as shown in Fig. 1(d).

5. Collinear bidirectional stripes

We call a state a collinear bidirectional stripe (ClBS) if it consists of two orthogonal stripes with parallel spin orientations, that is, if the nonzero components of $\vec{\mathcal{S}}_\mathbf{q}$ in Eq. (14) are

given by

$$\vec{\mathcal{S}}_x = \vec{\mathcal{S}}_y = S_0 \begin{pmatrix} 1 \\ 0 \\ 0 \end{pmatrix}, \tag{19}$$

where S_0 is a real constant. In real space, this corresponds to

$$\langle \vec{S}_j \rangle = S_0 \begin{pmatrix} \cos(\mathbf{Q}_x \cdot \mathbf{r}_j) + \cos(\mathbf{Q}_y \cdot \mathbf{r}_j) \\ 0 \\ 0 \end{pmatrix}. \tag{20}$$

This phase has charge modulations in both x and y directions, proportional to $[\cos(\mathbf{Q}_x \cdot \mathbf{r}_j) + \cos(\mathbf{Q}_y \cdot \mathbf{r}_j)]^2$, as displayed in Fig. 1(e).

6. Coplanar bidirectional stripes

We call a state a coplanar bidirectional stripe (CpBS) if it consists of two orthogonal stripes with orthogonal spin orientations, that is, if we find two **q** modes of the form

$$\vec{\mathcal{S}}_x = S_0 \begin{pmatrix} 1 \\ 0 \\ 0 \end{pmatrix}, \quad \vec{\mathcal{S}}_y = S_0 \begin{pmatrix} 0 \\ 1 \\ 0 \end{pmatrix}, \tag{21}$$

with S_0 being a real constant. In the real-space representation this corresponds to

$$\langle \vec{S}_j \rangle = S_0 \begin{pmatrix} \cos(\mathbf{Q}_x \cdot \mathbf{r}_j) \\ \cos(\mathbf{Q}_y \cdot \mathbf{r}_j) \\ 0 \end{pmatrix}. \tag{22}$$

This phase also has charge modulations in both x and y directions, proportional to $[\cos(\mathbf{Q}_x \cdot \mathbf{r}_j)]^2 + [\cos(\mathbf{Q}_y \cdot \mathbf{r}_j)]^2$, as shown in Fig. 1(f).

7. Beat states

Sometimes we find states whose dominant **q** components take the form (up to a lattice rotation) $\mathbf{Q}_x = (\pi - 2\pi\eta, \pi)$ and $\mathbf{Q}'_x = (\pi - 2\pi\eta', \pi)$ with $\eta \neq \eta'$. As shown in Fig. 1(g), in these states there are unidirectional charge modulations, and the spin patterns usually show beatlike modulations, since the spin components are sums of cosines with different wave numbers and phases. As we will discuss in more detail in Sec. III A 3, we attribute these states to finite-size effects. In fact, they arise due to the fact that the "optimal" incommensurability η_{opt} lies in between η and η', which is, however, not allowed by the finite size of the system [cf. Eq. (12)]. In the thermodynamic limit, where any (real) value of η is permitted, we expect these states to converge to a pure stripe or spiral phase.

8. Other collinear orders

In some cases all the spins are ordered collinearly (that is, $\langle \vec{S}_j \rangle \propto \hat{n}$ with $\hat{n}$ being a constant unit vector), but not in the shape of Néel order, stripe order, or collinear bidirectional stripes. In these phases, the amplitude of the spins varies spatially, and as a result we also obtain a charge modulation. As noted in Ref. [18], these states may be replaced by stripe states in the thermodynamic limit. Indeed, the lattice sizes treated in our calculations are too small to resolve stripes with wave vectors $\mathbf{Q}$ close to (π, π), so that the system prefers to

order in a more complex manner. Such a state, sketched in Fig. 1(h), can be viewed as a kind of stripe order where the lines of constant density, instead of lying parallel to the x (or y) direction, close onto themselves, forming a ring. In these cases, we find several nonzero components of $\vec{\mathcal{S}}_{\mathbf{q}}$.

9. Strange orders

In some cases we cannot classify a state by the previously described orders. Such states do not exhibit a simple structure in momentum space and often show complex charge patterns. In the following we will refer to these orders as "strange order." In the majority of cases, but not always, their spin order is coplanar. An example is sketched in Fig. 1(i). We expect these strange states to disappear in the thermodynamic limit, as we will discuss more exhaustively in Sec. III A 3.

III. RESULTS

We now present our results. Unrestricted real-space Hartree-Fock calculations have been carried out on a 20×20 lattice, supplemented by a few calculations on larger lattices (up to 48×48) to analyze finite-size effects. Except for one case, we chose $\mathcal{N}_x = \mathcal{N}_y$ to not bias the system towards orders breaking point group symmetries.

We chose a moderate coupling strength $U = 3t$ in all calculations. This choice is motivated by two reasons. First, within the Hartree-Fock approximation, $U = 3t$ is strong enough to obtain magnetic order for all our choices of t' for both hole and electron doping. For weaker interactions, magnetic order may be restricted to a small hole-doping regime around Van Hove filling. Second, it is weak enough to obtain (qualitatively) plausible results from the Hartree-Fock approximation. At strong coupling, the Hartree-Fock approximation yields magnetic ordering patterns which are most likely artifacts of the approximation, so that it is not worthwhile discussing them.

For the hopping amplitudes we consider three distinct ratios t'/t, namely, 0, -0.15, and -0.3. The first one corresponds to the so-called "pure" Hubbard model, which has been the preferred choice in many numerical studies, while the second and third choices are ratios that are frequently used for a realistic modeling of the cuprate superconductors belonging to the lanthanum strontium copper oxide (LSCO) and yttrium barium copper oxide (YBCO) families, respectively. Note, however, that the interaction strength in cuprates is much larger than our choice $U = 3t$.

We performed a temperature and filling scan with steps of 0.01 in T/t and n. We classified the converged states according to the classification scheme described in Sec. II B. In Appendix B, we specify the criteria and numerical method employed to achieve this. In most cases the system converges to a unique (modulo symmetries) state independently of the initial conditions. To reduce the risk of converging to a metastable state corresponding to a local but not global minimum of the free energy, we repeated the calculations for each point (n, T) starting five times from a random configuration and then from the converged solutions at the neighboring points $(n \pm 0.01, T)$ and $(n, T \pm 0.01t)$. In the rare cases where the iterations converged to inequivalent states, we retained the state with the lowest free energy.
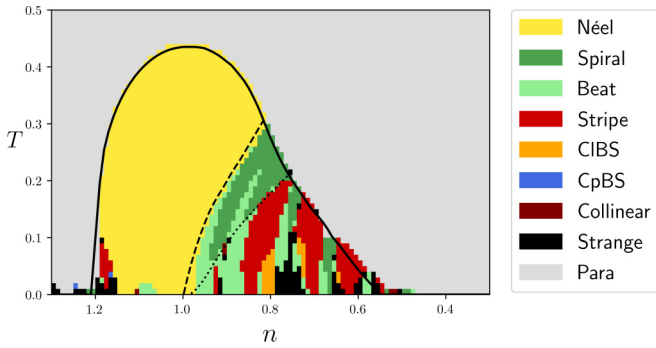
FIG. 2. Phase diagram for $U = 3t$ and $t' = -0.15t$. The colors label the states resulting from the real-space calculation on a 20×20 lattice. The black lines were obtained from calculations in momentum space in the thermodynamic limit. The solid black line indicates the transition temperature T^* separating the paramagnetic (para) regime from the magnetically ordered regime, the dashed black line indicates the transition between Néel and non-Néel spiral order, and the dotted black line indicates the divergence of the charge susceptibility in the spiral state.

For Néel and, more generally, spiral states, the mean-field equations can be solved in the thermodynamic limit, using a momentum-space representation [6–9,11], and the stability of the spiral states in the thermodynamic limit can be probed by computing the spin and charge susceptibilities [48,49]. We exploit this complementary approach to benchmark and to interpret the results from the real-space finite-size calculations.

A. Results for $t' = -0.15t$

We start by presenting exemplary results for a next-nearest-neighbor hopping $t' = -0.15t$ at intermediate interaction strength $U = 3t$. In Sec. III B, we show results for $t' = 0$ and $t' = -0.3t$.

1. Phase diagram

In Fig. 2, we show the mean-field phase diagram as a function of the particle density n and the temperature T. The colors label the states resulting from the real-space calculation on a 20×20 lattice, while the black lines were obtained from calculations in momentum space in the thermodynamic limit. The transition temperature T^* obtained from the momentum-space calculation (solid black line) is very close to the transition temperature obtained for the finite system. Since electronic correlations are neglected, the Hartree-Fock approximation overestimates the size of the critical dopings at the edges of the ordered regime. For the same parameters, significantly smaller critical values are found in a renormalized mean-field theory with effective interactions obtained from a functional renormalization group flow [13].

For densities close to half filling, we find a Néel-ordered region, which at $n = 1$ extends up to a critical temperature $T^* \approx 0.43t$. With few exceptions, Néel order is also obtained in the entire electron-doped region (for $n > 1$). Not only T^*, but also the boundary of the Néel-ordered region inside the magnetic regime obtained from the momentum-space calculation (dashed line) agrees very well with the real-space finite-size calculation.

On the hole-doped side, the momentum-space calculation in the thermodynamic limit yields a regime of stable spiral order with a continuously varying incommensurability η between the dashed and the dotted black lines in Fig. 2. In the real-space calculation on the 20×20 lattice, the spiral regime is split into spiral and beat order regions, where the incommensurabilities in the spiral regions are either $\eta = 0.05$ (close to the Néel region) or $\eta = 0.1$.

At densities and temperatures where we observe beat states it is energetically more costly for the system to order as a spiral state with the discrete incommensurabilities 0.05 or 0.1 allowed on the 20×20 lattice. We will discuss this point further in Sec. III A 3. Since intermediate ordering vectors are prohibited due to the periodic boundary conditions, the system orders in a beat-ordered pattern. Looking at the wave vectors of the Fourier modes $\vec{S}_{\mathbf{q}}$ in these states, one finds $\mathbf{Q}_1 = (\pi - 2\pi \frac{1}{20}, \pi)$ and $\mathbf{Q}_2 = (\pi - 2\pi \frac{1}{10}, \pi)$. We therefore expect the beat states to be artifacts of the finite system size. We recalculated the magnetic and charge orders in the beat region between the spiral states on a 40×40 lattice and found that beat order is indeed replaced by spiral order with an intermediate wave vector $\mathbf{Q} = (\pi - 2\pi \frac{3}{40}, \pi)$. Hence the real-space calculation is consistent with a spiral phase with a smoothly varying η (increasing upon decreasing density and temperature) in the thermodynamic limit, as suggested by the momentum-space analysis.

Below the dotted line in Fig. 2, and for any temperature at densities below $n \approx 0.75$, spiral states exhibit negative (for some wave vectors) spin and charge susceptibilities, and are thus unstable. In this region we find extended phases with stripes and other collinear orders. The stripe region is split into several domains with distinct incommensurabilities: $\eta = 0.05$ for densities $n \approx 0.93$, $\eta = 0.1$ for densities close to $n \approx 0.82$, $\eta = 0.15$ for densities around 0.7, and $\eta = 0.2$ near $n \approx 0.62$. These stripe regimes are separated by intermediate regions of beat-ordered and strange phases, where the predominant wave vectors are the ones of the two adjacent stripe regimes. In these intermediate regions, we recalculated the states on a 40×40 lattice for a few (n, T) pixels and found stripes with intermediate values of η. This confirms the hypothesis that beat and strange states are just artifacts of the finite system size.

The stability of the spiral state can be probed in the thermodynamic limit by computing the spin and charge susceptibilities in momentum space in the random phase approximation (RPA), following Refs. [48,49]. Joint divergences are found for the in-plane spin susceptibility and for the charge susceptibility. The dotted black line in Fig. 2 marks the line at which the charge susceptibility χ_C diverges. For temperatures below that line, one obtains an unphysical negative charge susceptibility. The divergence of the charge susceptibility, occurring for a wave vector of the form $\mathbf{Q}_C = (\pm\bar{q}_x, 0)$ for a spiral with wave vector $(\pi - 2\pi\eta, \pi)$, is always concomitant with a divergence of the spin susceptibility in the plane in which the spirals lie. This indicates the instability of the spiral state towards a state displaying a charge modulation and a rearrangement of the spins in the plane. The fact that the line of diverging charge susceptibility coincides with the transition from spiral order to stripe order confirms the idea that stripes emerge as an instability of the spiral states [4,8,50]. We show
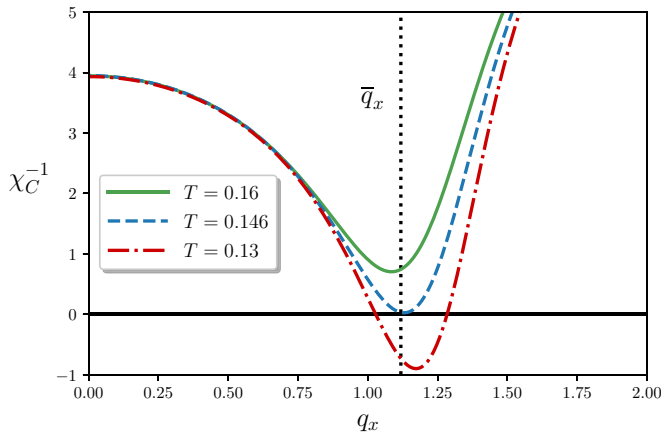
FIG. 3. Inverse of the RPA charge susceptibility χ_C^{-1} along the momentum line $\mathbf{q} = (q_x, 0)$ for $n = 0.85$, $t' = -0.15t$, and $U = 3t$. The divergence of χ_C occurs at $T \approx 0.146$. For these parameters, we find an optimal wave vector $\mathbf{Q}$ of the form $(\pi - 2\pi\eta, \pi)$ with $\eta = 0.089$. We show χ_C^{-1} for three different temperatures. χ_C becomes negative for $T < 0.146$.

χ_C for the density $n = 0.85$ and temperatures in the vicinity of the spiral-stripe transition in Fig. 3. Close to the transition, we find that $\mathbf{Q}_C$ is given by twice the optimal spiral wave vector $\mathbf{Q}$ modulo a reciprocal lattice vector, indicating the onset of stripe order with a charge modulation wave vector $2\mathbf{Q}$, and a spin modulation with wave vector $\mathbf{Q}$, in agreement with Eq. (10).

For densities below $n \approx 0.75$ we observe a *direct* second-order transition from the paramagnetic state to a stripe state. This occurs without a diverging charge susceptibility at the critical temperature (only the magnetic susceptibility diverges), as the charge modulation in the stripe phase is a second-order effect, induced by the spin ordering [47]. In the momentum-space mean-field calculation with spiral order, we observe in this regime diverging charge and in-plane spin susceptibilities at any temperature below T^*, that is, as soon as the spiral order parameter forms. This shows that spiral order is not even metastable in the stripe regime.

2. Magnetization

In Fig. 4, we plot the average magnetization per site,

$$m = \frac{1}{\mathcal{N}} \sum_j \sqrt{\langle S_j^x \rangle^2 + \langle S_j^y \rangle^2 + \langle S_j^z \rangle^2}. \qquad (23)$$

Within the limitations due to the discrete grid for n and T, the transitions from the paramagnetic state to Néel, spiral, and stripe order look all continuous. A continuous phase transition from a paramagnetic state to a collinear spin configuration is consistent with the Landau theory of phase transitions [47]. The magnetization is maximal near half filling, as expected. We see slight dips in the average magnetization near the transition from stripe to spiral phases as well as in some of the beat phases. We believe that this originates from the finite size of the system, since the scale of the dips is approximately the same as the change in the value of the magnetization between calculations on a 40×40 and a 20×20 lattice.
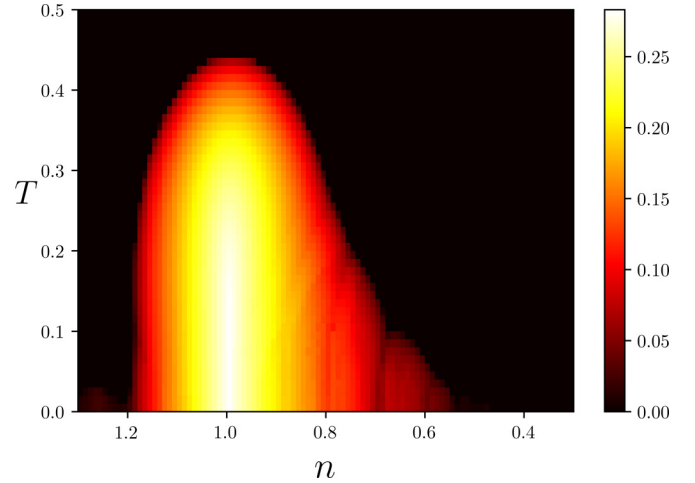

FIG. 4. Average magnetization m for $U = 3t$ and $t' = -0.15t$, calculated on a 20×20 lattice.

3. Energetic analysis

To further clarify which phases found in our finite-size calculation will survive in the thermodynamic limit, we compared the finite-size free energy F_{fs} from Eq. (9) with its counterpart F_{is} in an infinite system, where the magnetic states are restricted to Néel and spiral order. Focusing on the more interesting hole-doped regime, in Fig. 5 we show $F_{\text{fs}} - F_{\text{is}}$ for densities $0.65 \leqslant n \leqslant 1$. We only show the energy differences in the magnetic regime and set the energy differences in the paramagnetic phase to zero.

To set a reference scale, we note that the typical "condensation" energy $F_{\text{fs}} - F_{\text{pm}}$, where F_{pm} is the free energy obtained in the (unstable) paramagnetic mean-field solution, is of the order of $-0.05t$. The energy difference $F_{\text{fs}} - F_{\text{is}}$ is of the order
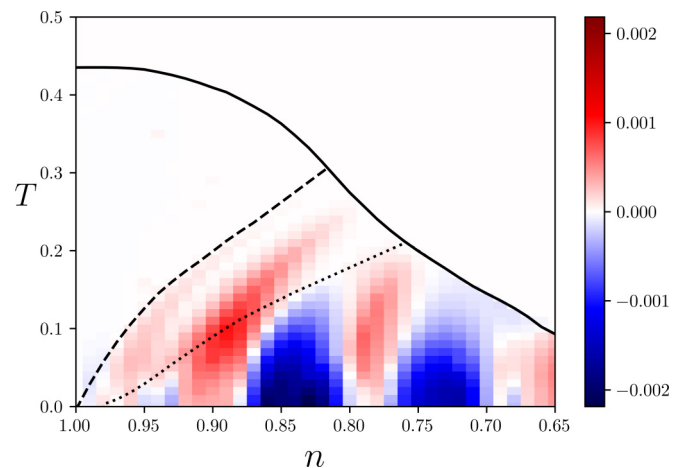

FIG. 5. Energy difference $F_{\text{fs}} - F_{\text{is}}$ between the real-space calculation on a 20×20 lattice and the momentum-space calculation in the thermodynamic limit. The model parameters are $U = 3t$ and $t' = -0.15$. The solid black line indicates T^*, the dashed black line indicates the transition between Néel and spiral order, and the dotted black line indicates the divergence of the charge susceptibility in the spiral state as obtained from the momentum-space mean-field code (as in Fig. 2).
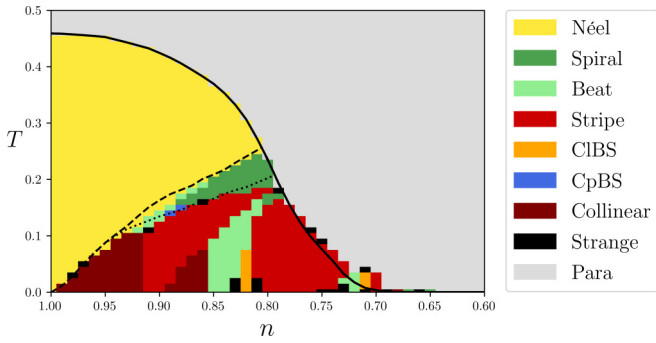
FIG. 6. Phase diagram for $U = 3t$ and $t' = 0$. The colors label the states obtained from a real-space calculation on a 20×20 lattice, and the black lines are defined as in Fig. 2. We show the phase diagram only for densities $n \leqslant 1$, since the system is particle-hole symmetric without next-to-nearest-neighbor hopping.

FIG. 7. Phase diagram for $U = 3t$ and $t' = -0.3t$. The colors label the states obtained from a real-space calculation on a 20×20 lattice, and the black lines are defined as in Fig. 2.

of a few percent of the total condensation energy. In regions where the real-space calculation yields Néel or spiral order, $|F_{fs} - F_{is}|$ is smaller than $10^{-5}t$.

In the beat state separating Néel and spiral order, one can see that $F_{fs} > F_{is}$, so the beat order is not expected to be stable in the thermodynamic limit, since the spiral state with optimal η has a lower free energy. The same applies to the beat states separating the two spiral regions with different pitches.

Below the dotted line in Fig. 5, we see a clear gain in energy in the centers of the stripe-ordered phases, indicating that stripe order can remain stable even in the thermodynamic limit. In the intermediate beat- and strange-ordered states, where stripe orders with **Q** near the optimal wave vector are prohibited by the periodic boundary conditions, we again find $F_{fs} > F_{is}$. Therefore the beat- and strange-ordered states will not be stable in the thermodynamic limit. As we know from the RPA susceptibilities that also spiral states are unstable in this regime, we expect stripe order with optimized intermediate wave vectors to take their place.

The analysis of the wave vectors of the beat states described in Sec. III A 1 together with the free-energy analysis above makes us believe that the beat states and the strange states are artifacts of the finite system size, and that in the thermodynamic limit the phase diagram consists only of a Néel-ordered dome around half filling accompanied by a spiral region and a stripe-ordered phase with smoothly varying wave vectors **Q** on the hole-doped side.

B. Results for $t' = 0$ and $-0.3t$

In this section, we show results similar to those of Sec. III A for next-to-nearest-neighbor hopping strengths $t' = 0$ and $t' = -0.3t$. We choose the same interaction strength $U = 3t$ and lattice size $\mathcal{N}_x = \mathcal{N}_y = 20$ as before.

1. Phase diagrams

The phase diagrams for $t' = 0$ and $t' = -0.3t$ are shown in Figs. 6 and 7, respectively. For $t' = 0$, the Hamiltonian is particle-hole symmetric, so that the hole- and electron-doped sides of the phase diagram look identical. Hence only the hole-doped side of the phase diagram is shown in Fig. 6.
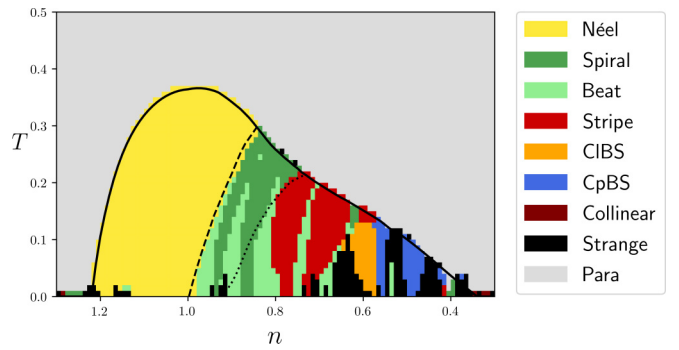
In the electron-doped regime, the phase diagram for $t' = -0.3t$ exhibits primarily a Néel-ordered regime, similar to the case $t' = -0.15t$, and in agreement with previous works [11,13,49].

On the hole-doped side the critical hole doping increases for larger $|t'|$, while T^* at half filling decreases. For all three values of t', we find a Néel-ordered regime also in the hole-doped regime in the proximity of half filling, shrinking, however, at low temperatures. For lower densities, all three phase diagrams exhibit an intermediate spiral regime. Analogously to Fig. 2, we also show the Néel-spiral transition line (dashed line) and the divergence of the charge susceptibility (dotted line) in the thermodynamic limit, as obtained from the momentum-space calculation. Similarly to the case $t' = -0.15t$, we find that the spiral states obtained on the 20×20 lattice are mostly located between these two lines. For $t' = 0$, all spiral states have an incommensurability of $\eta = 0.05$, whereas for $t' = -0.3t$, the spiral regime is again split into two regions, one with $\eta = 0.05$ and one with $\eta = 0.1$, separated by an intermediate beat region, in which the dominant wave vectors correspond to $\eta = 0.05$ and 0.1. The bigger $|t'|$ is, the larger is the area where spirals are the energetically favored state. While for $t' = 0$ the spiral area is a relatively thin strip below Néel order, for $t' = -0.3t$ the spiral region extends over a wide range of densities, and spiral order remains stable even in the ground state for densities down to $n = 0.91$. In the thermodynamic limit we expect a continuous evolution of η from $\eta = 0$ to $\eta \approx 0.1$ within the spiral region, and we expect the beat states to disappear from the phase diagram.

Below the dotted line, the phase diagrams exhibit stripe-ordered patches divided by intermediate beat states. For $t' = 0$, there is an $\eta = 0.05$ stripe region around $n \approx 0.88$ and an $\eta = 0.1$ stripe region around $n \approx 0.78$, separated by a beat region consisting of wave vectors with both values of η. For low doping, $n \gtrsim 0.92$, the system is collinearly ordered, but not in a perfect stripe pattern. The charge and spin patterns in this regime resemble those displayed in Fig. 1(h). As explained in Ref. [18], this is likely due to the fact that longer wavelengths cannot be accommodated on a 20×20 lattice. Indeed, when repeating the calculations on a 48×48 system, we found a stripe-ordered phase at a density of $n = 0.96$ for $T \leqslant 0.05$. The stripes we find in this regime do not appear in the shape
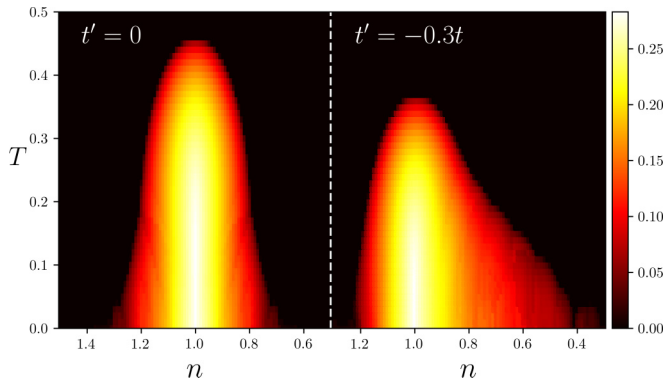
FIG. 8. Average magnetization per site for $U = 3t$ and either $t' = 0$ (left) or $t' = -0.3t$ (right) on a 20×20 lattice.

of a simple cosine as in Eq. (18), but their profile is generally sharper. We find two almost-half-filled regions separated by two hole-doped domain walls, which extend over five to ten sites each. Since the domain walls are usually perfectly parallel to the x or y axis, and all spins are collinear, we still refer to this region as stripe ordered. We expect that for larger lattices (but fixed density) the size of the domains remains roughly the same, being determined by the incommensurability, while the number of domains would increase. This differs from phase separation, where the lattice contains only two macroscopic domains (with distinct densities), which grow with the lattice size. For $t' = -0.3t$, there are two patches of stripe order, one centered around $n \approx 0.8$ corresponding to $\eta = 0.1$ and one centered around $n \approx 0.7$, with $\eta = 0.15$. Unlike in the $t' = 0$ and $-0.15t$ cases, there is a regime of collinear bidirectional stripes centered around filling $n = 0.6$, with $\eta = 0.2$, followed by two regions of coplanar bidirectional stripes with $\eta = 0.25$ and 0.30. These bidirectional stripe phases have a lower energy than the optimal spirals which we found from the momentum-space calculation, but to confirm that they remain stable in the thermodynamic limit and are not artifacts of the finite system size, we repeated the calculation for four (n, T) points in each of the three bidirectional stripe regimes for lattice sizes 28×28 and 40×40. In all cases, bidirectional stripe phases with a minimal free energy were found; so we believe that they will remain stable also in the thermodynamic limit.

At first sight, one may be surprised that the magnetically ordered regime becomes broader on the hole-doped side with increasing $|t'|$, although a next-nearest-neighbor hopping amplitude leads to a certain degree of frustration for antiferromagnetic order. At half filling, the critical temperature indeed shrinks with increasing $|t'|$. However, a negative t' also shifts the Van Hove filling (where the Fermi surface touches the saddle point of the dispersion) into the hole-doped regime, which leads to an enhancement of the bare spin susceptibility there. At weak coupling, this effect extends the magnetic regime to larger hole doping, compared with the case $t' = 0$.

2. Magnetization

In Fig. 8, we show the average magnetization per site for $t' = 0$ (left panel) and $t' = -0.3t$ (right panel). The magnetization is maximal near half filling. The transition from
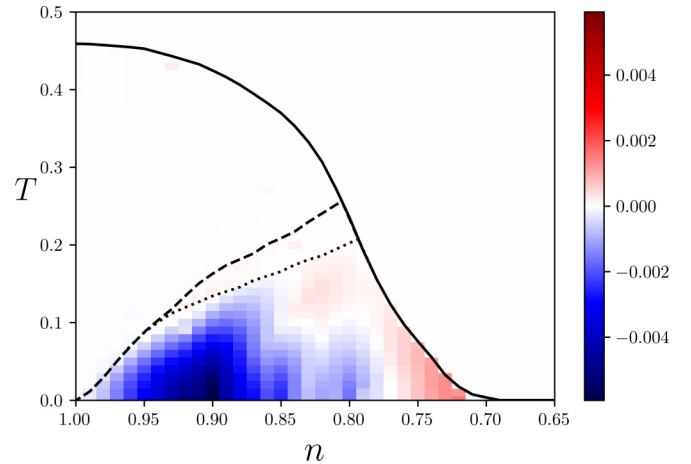
the paramagnetic phase to the ordered phases seems again smooth, as in the $t' = -0.15t$ case. However, due to discrete nature of our (n, T) grid, we cannot exclude weak first-order transitions.

3. Energy considerations

We have calculated the free-energy differences between the real-space calculation on a 20×20 lattice and the momentum-space calculation in the thermodynamic limit, $F_{\text{fs}} - F_{\text{is}}$, in the magnetic regime for $t' = 0$ and $t' = -0.3t$, analogously to Sec. III A 3. The results are shown in Figs. 9 and 10, respectively.

In both plots, we see that the differences in free energies in the Néel and spiral regimes are almost zero. There is generally an energy gain in the stripe-ordered phases and an energy loss in the beat- and strange-ordered phases, as for $t' = -0.15t$ in Sec. III A 3. For $t' = -0.3t$, we also see an energy gain in the collinear and coplanar bidirectional stripe phases at low fillings, compared with the spiral phase.
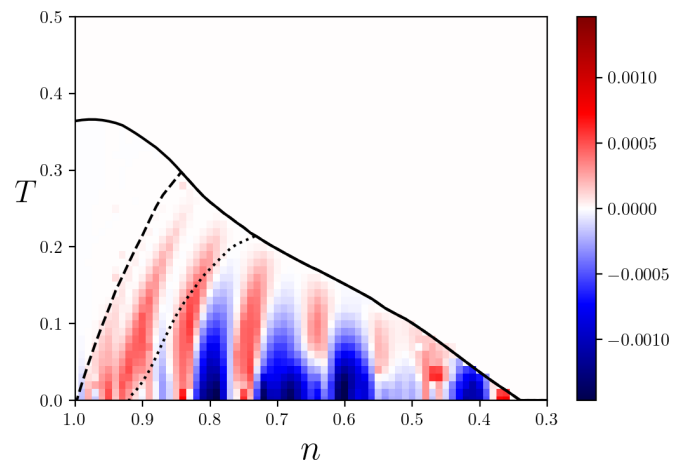

FIG. 9. Energy difference $F_{\text{fs}} - F_{\text{is}}$ between the real-space calculation on a 20×20 lattice and the momentum-space calculation in the thermodynamic limit as in Fig. 5, for $U = 3t$ and $t' = 0$.

FIG. 10. Energy difference $F_{\text{fs}} - F_{\text{is}}$ between the real-space calculation on a 20×20 lattice and the momentum-space calculation in the thermodynamic limit as in Fig. 5, for $U = 3t$ and $t' = -0.3t$.
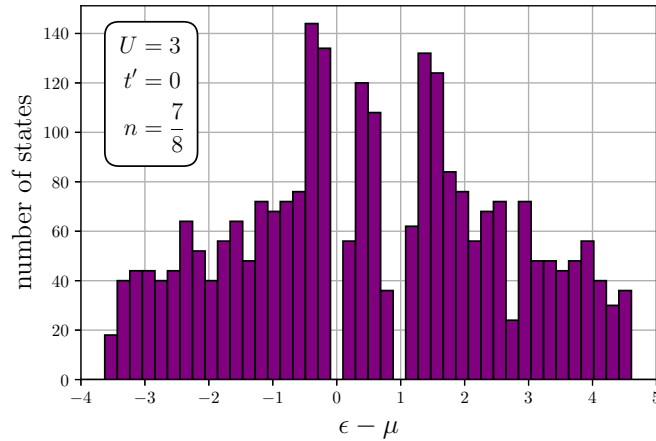
FIG. 11. Density of states histogram for $n = \frac{7}{8}$, $T = 0$, $t' = 0$, and $U = 3$, calculated on a 40×32 lattice. The states are counted in equidistant bins in the energy range between -4 and 5.

These observations reaffirm our expectation that the beat and strange states disappear from the phase diagram in the thermodynamic limit, while the Néel, spiral, and stripe states remain stable.

4. Density of states for $n = \frac{7}{8}$, $T = 0$, and $t' = 0$

A particular point in parameter space has received special attention in recent years: the ground state ($T = 0$) at a density $n = \frac{7}{8}$ for the two-dimensional Hubbard model with pure nearest-neighbor hopping. Exact numerical ground state techniques have provided fairly convincing evidence that for strong coupling the ground state is an insulating stripe state in this case [31,32]. Hence we investigate this special point in more detail, too, keeping, however, a moderate interaction strength $U = 3t$, in line with our Hartree-Fock approximation. To allow for a variety of distinct commensurabilities, and because stripes with wavelengths 8 and 16 were found by different numerical methods at $n = \frac{7}{8}$ [31–33,51,52], we work on an anisotropic lattice with $\mathcal{N}_x = 40$, $\mathcal{N}_y = 32$ in this case.

The solution of the real-space mean-field equations unambiguously yields unidirectional stripes with an incommensurability $\eta = \frac{1}{16}$ along the y axis. To see whether this stripe ground state is an insulator, we have computed the distribution of energy levels, which is a finite-size proxy to the density of states. In Fig. 11, we show a histogram of the distribution of the energy levels ϵ_l, shifted by the chemical potential (placed halfway between the highest occupied state and the lowest unoccupied state). The histogram is defined with equidistant bins between -4 and 5. We see that there are no energy levels close to the chemical potential, that is, there is a finite band gap with size $\Delta \approx 0.25t$. The state we find for this parameter set is therefore indeed an insulator. There are other insulating points in the ground state, but metallic behavior is much more frequent.

C. Phase diagrams in the thermodynamic limit

Collecting the insights gained from the real-space and momentum-space solutions of the mean-field equations

discussed above, we now present our expectation for the mean-field phase diagrams of the two-dimensional Hubbard model in the thermodynamic limit. These final (n, T) phase diagrams for $U = 3t$ and $t' = 0, -0.15t$, and $-0.3t$ are shown in Figs. 12–14, respectively.

Based on the energy considerations and the analysis of the dominant wave vectors in each phase, we concluded that neither beat nor strange states will remain stable in the thermodynamic limit. There is no indication that the Néel and spiral states are unstable within the regions shown in the phase diagrams. The divergence of the charge susceptibility at the low-temperature boundary of the spiral regime (dotted line in Figs. 12–14) indicates a transition to a stripe state, which is indeed found within the real-space calculation whenever the optimal wave vector can be accommodated on the finite lattice.

At zero temperature, the Néel state is stable for densities $n \geqslant 1$ for $t' \leqslant -0.15t$, and a spiral phase extends from half
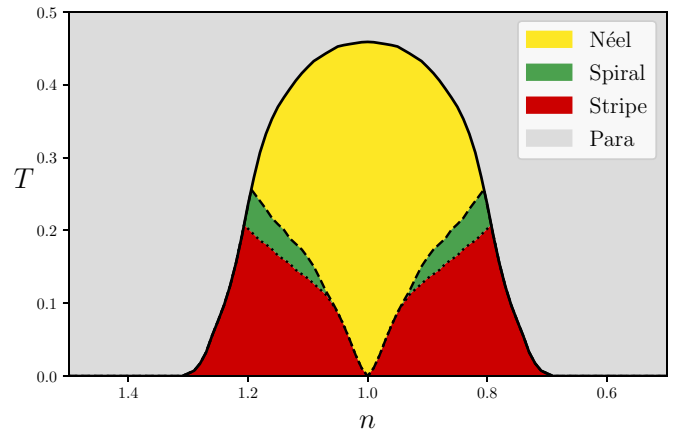

FIG. 12. (n, T) phase diagram for $t' = 0$ and $U = 3t$ in the thermodynamic limit with Néel, spiral, and unidirectional stripe order. Because of the Hamiltonian's particle-hole symmetry, this phase diagram is symmetric.
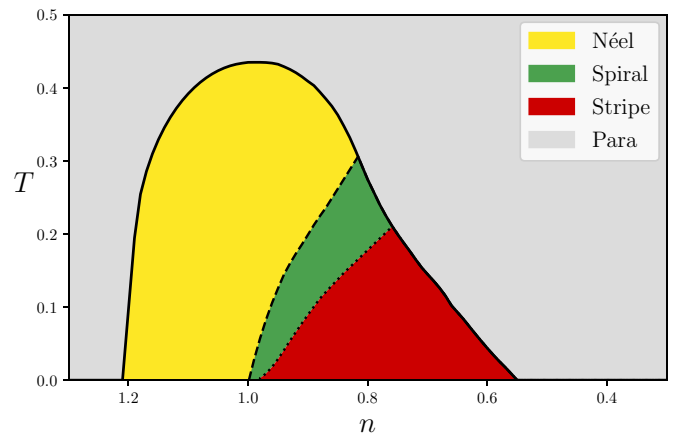

FIG. 13. (n, T) phase diagram for $t' = -0.15t$ and $U = 3t$ in the thermodynamic limit with Néel, spiral, and unidirectional stripe order. There is a narrow spiral regime at small hole doping even at $T = 0$.
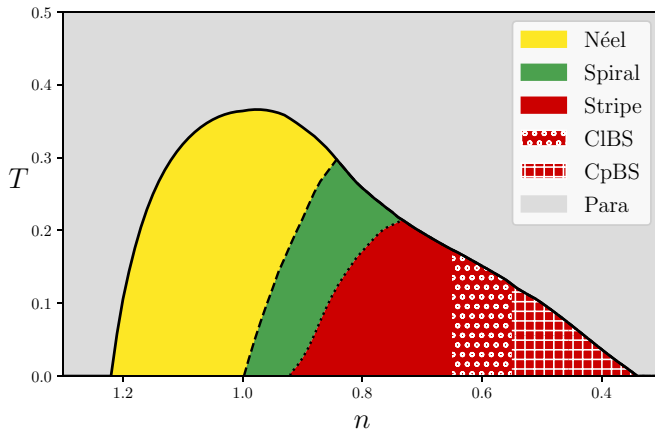
FIG. 14. (n, T) phase diagram for $t' = -0.3t$ and $U = 3t$ in the thermodynamic limit with Néel, spiral, and stripe order. Its topology is similar to the $t' = -0.15$ case, but the spiral regime is larger, especially at low temperatures, and besides unidirectional stripes there are also regimes of collinear and coplanar bidirectional stripes.

filling to a hole doping $p = 0.02$ for $t' = -0.15t$, and to $p = 0.09$ for $t' = -0.3t$, while for larger hole doping stripe order prevails. For $t' = 0$ the Néel ground state is unstable toward stripe order at any finite doping. For $t' = -0.3t$ we also found collinear bidirectional stripes and coplanar bidirectional stripes on the 20×20 lattice, which remain stable also for larger systems. It is difficult to determine the exact domain borders of the three stripe variants in the thermodynamic limit. On the 20×20 lattice, the system exhibits ClBS order in the doping range $p \approx 0.35$–0.45 and CpBS order in the doping range $p \approx 0.45$–0.65.

IV. CONCLUSION

We have performed an unbiased mean-field analysis of magnetic and charge orders in the two-dimensional Hubbard model, both at zero and finite temperature. Fully unrestricted Hartree-Fock calculations on large finite lattices (from 20×20 to 48×48) have been complemented by momentum-space solutions restricted to Néel and circular spiral states in the thermodynamic limit. The Hubbard interaction was fixed at the moderate value $U = 3t$, while three distinct ratios of next-nearest-neighbor to nearest-neighbor hopping amplitudes were considered: $t'/t = 0$, -0.15, and -0.3. The magnetic states were classified by a systematic scheme based on the dominant Fourier components $\vec{\mathcal{S}}_\mathbf{q}$ of the spin texture $\langle \vec{S}_j \rangle$. All but Néel and circular spiral states entail charge, in addition to spin, order.

On the finite lattices a whole zoo of magnetic states has been found, some of which look quite messy. However, comparing solutions on different lattices, analyzing the condensation energies, and comparing these states with Néel and spiral solutions in the thermodynamic limit, we could show that the more complex states are finite-size artifacts, which are related to the limited choice of ordering wave vectors on finite lattices. On a finite lattice with periodic boundary conditions the optimal wavelength of a spin (and charge) density wave can be accommodated only if the lattice size is an integer

multiple of that wavelength. If the mismatch is too big, the magnetic and charge orders assume complex structures, for example, with charge stripes closing to a ring [18]. These "compromise" states disappear as the lattice size increases.

In the thermodynamic limit, only Néel, circular spiral, and stripe states are present. The latter are usually unidirectional, but can be bidirectional for $t' = -0.3t$. All phases are homogeneous; we find no evidence for macroscopic phase separation. The final (n, T) phase diagrams for $t' = 0$, $-0.15t$, and $-0.3t$ are shown in Figs. 12–14, respectively. The boundaries of the Néel and spiral regimes can be determined with high accuracy directly in the thermodynamic limit from the momentum-space solution of the mean-field equations restricted to these phases, complemented by an analysis of the RPA charge and spin susceptibilities. The susceptibilities are positive for all wave vectors inside the Néel and spiral domains, and divergences occur exclusively due to the Goldstone modes [49,53]. The charge distribution is uniform in the entire Néel and spiral regime. The instability of the spiral state toward stripe order is marked by a divergence of the charge susceptibility. On general grounds, one would expect either a first-order transition from circular spiral to stripe before the charge susceptibility diverges, or an intermediate elliptical spiral phase [47]. However, our data indicate that the transition from spiral to stripe order occurs close to the line where the charge susceptibility diverges. We did not detect any intermediate elliptical spiral states, but we might have missed them due to tiny energy differences and finite size limitations. Preliminary calculations for commensurate ordering wave vectors in the thermodynamic limit indicate the presence of elliptical spirals between the circular spiral and the stripe regimes.

In the ground state, Néel order is limited to half filling if $t' = 0$, and extends to the electron-doped regime ($n > 1$) for $t' = -0.15t$ and $t' = -0.3t$. Néel order is replaced by spiral or stripe order for arbitrarily small hole doping at $T = 0$. Note, however, that Néel order can be stable for low hole doping and negative t' for weaker bare or renormalized interactions [6,7,13]. In most parts of the phase diagram, the spatial dependence of the spin and charge patterns is well described by simple trigonometric functions (sine and cosine) with few wave vectors. Only for $t' = 0$ and low doping does a sharp real-space profile with antiferromagnetic domains separated by hole-rich domain walls develop, corresponding to a sizable contribution from higher harmonics in a Fourier decomposition. While doped Néel and spiral states are always metallic, we find some insulating spots in the stripe regime, in particular for the intensively studied special case $t' = 0$ and $n = \frac{7}{8}$, in qualitative agreement with exact numerical calculations on finite lattices [31–33,51,52].

A static mean-field calculation is clearly not applicable to the physics of cuprate superconductors, which should be described by the Hubbard model (or extensions) at strong coupling. Nevertheless, some broad features we obtain are in line with experimental observations in cuprates [54]: Néel order at and near half filling, with a broader Néel regime for electron-doped cuprates, incommensurate magnetic correlations with wave vectors of the form $\mathbf{Q} = (\pi - 2\pi\eta, \pi)$ for hole-doped cuprates, and charge and/or stripe order for some of them.

The mean-field analysis presented in this paper could be extended in various directions. At moderate coupling, substantial quantitative improvement could be achieved, and the interplay with d-wave pairing could be studied by using a renormalized mean-field theory where effective couplings obtained from a functional renormalization group flow are used instead of the bare Hubbard interaction [13,55,56]. An extension of dynamical mean-field theory (DMFT) to inhomogeneous systems, the iDMFT [57], can capture arbitrary spin and charge order patterns at strong coupling. Inhomogeneous DMFT studies of spin and charge order in the two-dimensional Hubbard model have already been performed [24,26,28], but so far only at zero temperature and for pure nearest-neighbor hopping. Finally, one could take spin fluctuations into account to replace the magnetic state with long-range order by a fluctuating magnet with short-range (and possibly topological) order by extending SU(2) gauge theories with Néel- and spiral-ordered chargons [40–42] to stripes.

The code we developed to perform the calculations is publicly available [58].

ACKNOWLEDGMENTS

APPENDIX A: COMPUTATIONAL DETAILS

We provide here additional information about the procedure we used to obtain converged states for a given set of parameters U, t', T, n, $\mathcal{N}_x$, and $\mathcal{N}_y$.

1. Mixing

To improve the convergence of the iterative scheme, we employ a linear mixing between each iteration. Instead of constructing the new Hamiltonian with the expectation values as obtained from Eq. (6) or (7), we instead use 60% of the new expectation values and keep 40% of the current ones. The mixing has proven to be essential to ensure convergence and avoid getting trapped in local minima.

2. Convergence criteria

We consider a state to be converged either if all the parameters $\Delta_{j\alpha}$ from Eq. (3) change by less than 10^{-8} between two iterations, or after 3500 iterations. Reducing the threshold value below 10^{-8} does not affect the results. The second convergence criterion was chosen to ensure that the computation will eventually terminate. A total of 3500 iterations is usually more than enough to obtain a state which is already clearly defined and can be classified as the same type of magnetic order as the fully converged state. Since we additionally calculated each (n, T) pixel multiple times with various random initial conditions, we are confident to have classified the true global minimum for each parameter set.

3. Scaling of the code with $\mathcal{N}$

In each iteration the step which takes by far most of the time is the diagonalization of the quadratic Hamiltonian, Eq. (4). This matrix diagonalization scales roughly as $\mathcal{N}^3$. The matrix is very sparse; so there are more efficient algorithms for obtaining the lowest eigenstates. However, we make use of *all* the eigenvalues and eigenvectors, and most of the commonly used eigensolvers for sparse matrices are only efficient to obtain a few of the lowest-energy eigenstates.

APPENDIX B: CLASSIFICATION OF STATES

We here give an overview of how we classify states on the 20×20 lattice via the Fourier components $\vec{\mathcal{S}}_{\mathbf{q}}$ introduced in Eq. (11). The classification is usually not too sensitive to the chosen thresholds and the used norms.

If we find that

$$\frac{1}{\mathcal{N}} \sqrt{\sum_{\mathbf{q}} |\vec{\mathcal{S}}_{\mathbf{q}}|^2} < 2.5 \times 10^{-7}, \tag{B1}$$

we classify the state as paramagnetic.

To classify the other states, we first note that the $\vec{\mathcal{S}}_{\mathbf{q}}$ with the largest norms usually correspond to wave vectors of the form

$$\mathbf{q}_x = (\pi - 2\pi \eta_x, \pi),$$
$$\mathbf{q}_y = (\pi, \pi - 2\pi \eta_y), \tag{B2}$$

with variable $\eta_{x,y}$. Note that we use the notation $\mathbf{q}_x$ ($\mathbf{q}_y$) to indicate the *class* of vectors of the form (B2), while $\mathbf{Q}_x$ ($\mathbf{Q}_y$) denotes a *single* wave vector with a fixed value of η_x (η_y). We also checked for diagonal order of the form $\mathbf{q}_{xy} \equiv (\pi - 2\pi\eta, \pi - 2\pi\eta)$; however, we found almost no states with these modes as dominant contributions [less than 40 (n, T) pixels in all three phase diagrams], and when we found them, the order did not remain stable when repeating the calculations on a 40×40 lattice.

To determine the ℓ dominant $\mathbf{q}$ modes, labeled as $\mathbf{q}_i$, of a state, we used the condition

$$\frac{\sqrt{\sum_{i=1}^{l} |\vec{\mathcal{S}}_{\mathbf{q}_i}|^2 + |\vec{\mathcal{S}}_{-\mathbf{q}_i}|^2}}{\sqrt{\sum_{\mathbf{q} \in \{\mathbf{q}_x, \mathbf{q}_y\}} |\vec{\mathcal{S}}_{\mathbf{q}}|^2}} > 95\%, \tag{B3}$$

where $\mathbf{q}_1 \cdots \mathbf{q}_l$ are the subset of wave vectors $\{\mathbf{q}_x, \mathbf{q}_y\}$ with the largest amplitudes $|\vec{\mathcal{S}}_{\mathbf{q}_i}|$ in descending order, and we always considered the $\mathbf{q}$ and $-\mathbf{q}$ modes as a single mode, since $\vec{\mathcal{S}}_{-\mathbf{q}} = \vec{\mathcal{S}}_{\mathbf{q}}^*$.

For most states we find that only one or two modes have a significant Fourier component. If three or more modes contribute, we label the state as displaying either strange or other collinear order. To check whether a state is collinearly ordered, we first rotate all $\vec{\mathcal{S}}_{\mathbf{q}}$ so that the real part of $\vec{\mathcal{S}}_{\mathbf{q}}$ with the biggest norm points in the x direction. We then say that a state is collinear if

$$\frac{1}{\mathcal{N}} \sqrt{\sum_{\mathbf{q}} |\mathcal{S}_{\mathbf{q}}^y|^2} < 2.5 \times 10^{-7}, \tag{B4}$$

and the same for $\mathcal{S}_{\mathbf{q}}^z$. We proceed analogously if the $\mathbf{q}$ modes of the $\mathbf{q}_x$ or $\mathbf{q}_y$ form make up less than 70% of the total norm of the Fourier transformation, that is, if

$$\frac{\sqrt{\sum_{\mathbf{q} \in \{\mathbf{q}_x, \mathbf{q}_y\}} |\vec{\mathcal{S}}_{\mathbf{q}}|^2}}{\sqrt{\sum_{\mathbf{q}} |\vec{\mathcal{S}}_{\mathbf{q}}|^2}} < 70\%. \tag{B5}$$

If we find only two contributing modes $\mathbf{Q}_1, \mathbf{Q}_2 \in \{\mathbf{q}_x, \mathbf{q}_y\}$, we proceed as follows.

If $\mathbf{Q}_1$ and $\mathbf{Q}_2$ are both in $\{\mathbf{q}_x\}$ or both in $\{\mathbf{q}_y\}$, we consider the state a beat state. Typically, $\mathbf{Q}_1$ and $\mathbf{Q}_2$ correspond to adjacent allowed values of η.

If $\mathbf{Q}_1$ and $\mathbf{Q}_2$ have the form $\mathbf{Q}_1 = (\pi - 2\pi\eta, \pi)$ and $\mathbf{Q}_2 = (\pi, \pi - 2\pi\eta)$, we rotate the vectors so that the real part of $\vec{\mathcal{S}}_{\mathbf{Q}_1}$ points in the x direction and then divide each vector by the norm of $\vec{\mathcal{S}}_{\mathbf{Q}_1}$. We then check how the $\vec{\mathcal{S}}_{\mathbf{Q}_1}$ are oriented relative to each other with an error tolerance of 5×10^{-3}. For example, for coplanar bidirectional stripes (see Sec. II B), we check whether $\vec{\mathcal{S}}_{\mathbf{Q}_1} \cdot \vec{\mathcal{S}}_{\mathbf{Q}_2} = 0$, $\mathcal{S}_{\mathbf{Q}_1}^y = \mathcal{S}_{\mathbf{Q}_1}^z = 0$, and $|\vec{\mathcal{S}}_{\mathbf{Q}_1}| = |\vec{\mathcal{S}}_{\mathbf{Q}_2}|$, each equality up to a tolerance of 0.5%. We proceed analogously for collinear bidirectional stripes. If we find different orientations of $\vec{\mathcal{S}}_{\mathbf{Q}_1}$ and $\vec{\mathcal{S}}_{\mathbf{Q}_2}$, as proposed in Ref. [46], we would classify the state as strange ordered, but this happens very rarely.

If we find only one contributing mode $\mathbf{Q}$, we proceed analogously to identify stripes or spirals. If additionally $\eta = 0$, we classify the state as a Néel antiferromagnet.

---

[1] D. J. Scalapino, A common thread: The pairing interaction for unconventional superconductors, Rev. Mod. Phys. **84**, 1383 (2012).

[2] D. P. Arovas, E. Berg, S. A. Kivelson, and S. Raghu, The Hubbard model, Annu. Rev. Condens. Matter Phys. **13**, 239 (2022).

[3] M. Qin, T. Schäfer, S. Andergassen, P. Corboz, and E. Gull, The Hubbard model: A computational perspective, Annu. Rev. Condens. Matter Phys. **13**, 275 (2022).

[4] B. I. Shraiman and E. D. Siggia, Spiral Phase of a Doped Quantum Antiferromagnet, Phys. Rev. Lett. **62**, 1564 (1989).

[5] B. I. Shraiman and E. D. Siggia, Excitation spectrum of the spiral state of a doped antiferromagnet, Phys. Rev. B **46**, 8305 (1992).

[6] A. V. Chubukov and D. M. Frenkel, Renormalized perturbation theory of magnetic instabilities in the two-dimensional Hubbard model at small doping, Phys. Rev. B **46**, 11884 (1992).

[7] A. V. Chubukov and K. A. Musaelian, Magnetic phases of the two-dimensional Hubbard model at low doping, Phys. Rev. B **51**, 12605 (1995).

[8] T. Dombre, Modulated spiral phases in doped quantum antiferromagnets, J. Phys. France **51**, 847 (1990).

[9] R. Frésard, M. Dzierzawa, and P. Wölfle, Slave-boson approach to spiral magnetic order in the Hubbard model, Europhys. Lett. **15**, 325 (1991).

[10] V. N. Kotov and O. P. Sushkov, Stability of the spiral phase in the two-dimensional extended $t-J$ model, Phys. Rev. B **70**, 195105 (2004).

[11] P. A. Igoshev, M. A. Timirgazin, A. A. Katanin, A. K. Arzhnikov, and V. Y. Irkhin, Incommensurate magnetic order and phase separation in the two-dimensional Hubbard model with nearest- and next-nearest-neighbor hopping, Phys. Rev. B **81**, 094407 (2010).

[12] P. A. Igoshev, M. A. Timirgazin, V. F. Gilmutdinov, A. K. Arzhnikov, and V. Y. Irkhin, Spiral magnetism in the single-band Hubbard model: the Hartree–Fock and slave-boson approaches, J. Phys.: Condens. Matter **27**, 446002 (2015).

[13] H. Yamase, A. Eberlein, and W. Metzner, Coexistence of Incommensurate Magnetism and Superconductivity in the Two-Dimensional Hubbard Model, Phys. Rev. Lett. **116**, 096402 (2016).

[14] A. Eberlein, W. Metzner, S. Sachdev, and H. Yamase, Fermi Surface Reconstruction and Drop in the Hall Number due to Spiral Antiferromagnetism in High-T_c Cuprates, Phys. Rev. Lett. **117**, 187001 (2016).

[15] J. Mitscherling and W. Metzner, Longitudinal conductivity and Hall coefficient in two-dimensional metals with spiral magnetic order, Phys. Rev. B **98**, 195126 (2018).

[16] P. M. Bonetti, J. Mitscherling, D. Vilardi, and W. Metzner, Charge carrier drop at the onset of pseudogap behavior in the two-dimensional Hubbard model, Phys. Rev. B **101**, 165142 (2020).

[17] H. J. Schulz, Domain walls in a doped antiferromagnet, J. Phys. France **50**, 2833 (1989).

[18] J. Zaanen and O. Gunnarsson, Charged magnetic domain lines and the magnetism of high-T_c oxides, Phys. Rev. B **40**, 7391 (1989).

[19] K. Machida, Magnetism in La_2CuO_4 based compounds, Phys. C (Amsterdam) **158**, 192 (1989).

[20] D. Poilblanc and T. M. Rice, Charged solitons in the Hartree-Fock approximation to the large-U Hubbard model, Phys. Rev. B **39**, 9749 (1989).

[21] H. J. Schulz, Incommensurate Antiferromagnetism in the Two-Dimensional Hubbard Model, Phys. Rev. Lett. **64**, 1445 (1990).

[22] M. Kato, K. Machida, H. Nakanishi, and M. Fujita, Soliton lattice modulation of incommensurate spin density wave in two dimensional Hubbard model -A mean field study, J. Phys. Soc. Jpn. **59**, 1047 (1990).

[23] G. Seibold, C. Castellani, C. Di Castro, and M. Grilli, Striped phases in the two-dimensional Hubbard model with long-range Coulomb interaction, Phys. Rev. B **58**, 13506 (1998).

[24] M. Fleck, A. I. Lichtenstein, E. Pavarini, and A. M. Oleś, One-Dimensional Metallic Behavior of the Stripe Phase in $La_{2-x}Sr_xCuO_4$, Phys. Rev. Lett. **84**, 4962 (2000).

[25] M. Fleck, A. I. Lichtenstein, and A. M. Oleś, Spectral properties and pseudogap in the stripe phases of cuprate superconductors, Phys. Rev. B **64**, 134528 (2001).

[26] M. Raczkowski and F. F. Assaad, Melting of stripe phases and its signature in the single-particle spectral function, Phys. Rev. B **82**, 233101 (2010).

[27] M. A. Timirgazin, M. A. Arzhnikov, and A. V. Vedyayev, Incommensurate spin-density wave in two-dimensional Hubbard model, Solid State Phenom. **190**, 67 (2012).

[28] R. Peters and N. Kawakami, Spin density waves in the Hubbard model: A DMFT approach, Phys. Rev. B **89**, 155134 (2014).

[29] K. Matsuyama and J. Greensite, Multiplicity, localization, and domains in the Hartree–Fock ground state of the two-dimensional Hubbard model, Ann. Phys. (Amsterdam) **442**, 168922 (2022).

[30] S. A. Kivelson, I. P. Bindloss, E. Fradkin, V. Oganesyan, J. M. Tranquada, A. Kapitulnik, and C. Howald, How to detect fluctuating stripes in the high-temperature superconductors, Rev. Mod. Phys. **75**, 1201 (2003).

[31] B.-X. Zheng, C.-M. Chung, P. Corboz, G. Ehlers, M.-P. Qin, R. M. Noack, H. Shi, S. R. White, S. Zhang, and G. K.-L. Chan, Stripe order in the underdoped region of the two-dimensional Hubbard model, Science **358**, 1155 (2017).

[32] M. Qin, C.-M. Chung, H. Shi, E. Vitali, C. Hubig, U. Schollwöck, S. R. White, and S. Zhang (Simons Collaboration on the Many-Electron Problem), Absence of Superconductivity in the Pure Two-Dimensional Hubbard Model, Phys. Rev. X **10**, 031016 (2020).

[33] H.-C. Jiang and T. P. Devereaux, Superconductivity in the doped Hubbard model and its interplay with next-nearest hopping t', Science **365**, 1424 (2019).

[34] F. Šimkovic IV, R. Rossi, and M. Ferrero, Two-dimensional Hubbard model at finite temperature: Weak, strong, and long correlation regimes, Phys. Rev. Res. **4**, 043201 (2022).

[35] B. Xiao, Y.-Y. He, A. Georges, and S. Zhang, Temperature Dependence of Spin and Charge Orders in the Doped Two-Dimensional Hubbard Model, Phys. Rev. X **13**, 011007 (2023).

[36] H. Q. Lin and J. E. Hirsch, Two-dimensional Hubbard model with nearest- and next-nearest-neighbor hopping, Phys. Rev. B **35**, 3359 (1987).

[37] W. Hofstetter and D. Vollhardt, Frustration of antiferromagnetism in the t-t'-Hubbard model at weak coupling, Ann. Phys. (Berlin) **510**, 48 (1998).

[38] E. Langmann and M. Wallin, Phase diagrams of the 2D $t - t' - U$ Hubbard model from an extended mean field method, J. Stat. Phys. **127**, 825 (2007).

[39] N. D. Mermin and H. Wagner, Absence of Ferromagnetism or Antiferromagnetism in One- or Two-Dimensional Isotropic Heisenberg Models, Phys. Rev. Lett. **17**, 1133 (1966).

[40] M. S. Scheurer, S. Chatterjee, W. Wu, M. Ferrero, A. Georges, and S. Sachdev, Topological order in the pseudogap metal, Proc. Natl. Acad. Sci. USA **115**, E3665 (2018).

[41] S. Sachdev, Topological order, emergent gauge fields, and Fermi surface reconstruction, Rep. Prog. Phys. **82**, 014001 (2019).

[42] P. M. Bonetti and W. Metzner, SU(2) gauge theory of the pseudogap phase in the two-dimensional Hubbard model, Phys. Rev. B **106**, 205152 (2022).

[43] A. Wietek, Y.-Y. He, S. R. White, A. Georges, and E. M. Stoudenmire, Stripes, Antiferromagnetism, and the Pseudogap in the Doped Hubbard Model at Finite Temperature, Phys. Rev. X **11**, 031007 (2021).

[44] A. Wietek, R. Rossi, F. Šimkovic, M. Klett, P. Hansmann, M. Ferrero, E. M. Stoudenmire, T. Schäfer, and A. Georges, Mott Insulating States with Competing Orders in the Triangular Lattice Hubbard Model, Phys. Rev. X **11**, 041013 (2021).

[45] F. Šimkovic IV, R. Rossi, A. Georges, and M. Ferrero, Origin and fate of the pseudogap in the doped Hubbard model, arXiv:2209.09237.

[46] S. Sachdev, H. D. Scammell, M. S. Scheurer, and G. Tarnopolsky, Gauge theory for the cuprates near optimal doping, Phys. Rev. B **99**, 054516 (2019).

[47] O. Zachar, S. A. Kivelson, and V. J. Emery, Landau theory of stripe phases in cuprates and nickelates, Phys. Rev. B **57**, 1422 (1998).

[48] A. P. Kampf, Collective excitations in itinerant spiral magnets, Phys. Rev. B **53**, 747 (1996).

[49] P. M. Bonetti and W. Metzner, Spin stiffness, spectral weight, and Landau damping of magnons in metallic spiral magnets, Phys. Rev. B **105**, 134426 (2022).

[50] A. Chubukov, Superconductivity in the 2D Hubbard model: yes, no, or maybe? Journal Club for Condensed Matter Physics, 2021, https://doi.org/10.36471/JCCM_February_2021_01.

[51] E. W. Huang, C. B. Mendl, H.-C. Jiang, B. Moritz, and T. P. Devereaux, Stripe order from the perspective of the Hubbard model, npj Quantum Mater. **3**, 22 (2018).

[52] L. F. Tocchio, A. Montorsi, and F. Becca, Metallic and insulating stripes and their relation with superconductivity in the doped Hubbard model, SciPost Phys. **7**, 021 (2019).

[53] P. M. Bonetti, Local Ward identities for collective excitations in fermionic systems with spontaneously broken symmetries, Phys. Rev. B **106**, 155105 (2022).

[54] B. Keimer, S. A. Kivelson, M. R. Norman, S. Uchida, and J. Zaanen, From quantum matter to high-temperature superconductivity in copper oxides, Nature (London) **518**, 179 (2015).

[55] J. Wang, A. Eberlein, and W. Metzner, Competing order in correlated electron systems made simple: Consistent fusion of functional renormalization and mean-field theory, Phys. Rev. B **89**, 121116(R) (2014).

[56] D. Vilardi, P. M. Bonetti, and W. Metzner, Dynamical functional renormalization group computation of order parameters and critical temperatures in the two-dimensional Hubbard model, Phys. Rev. B **102**, 245128 (2020).

[57] M. Potthoff and W. Nolting, Surface metal-insulator transition in the Hubbard model, Phys. Rev. B **59**, 2549 (1999).

[58] https://github.com/RoScholle/Zoo_Of_States/blob/main/RealSpace_HartreeFock_HubbardModel.py.